Effect of carbon on recrystallised microstructures and properties of CoCrFeMnNi-type high-entropy alloys

M. Klimova [*], D. Shaysultanov, A. Semenyuk, S. Zherebtsov, N. Stepanov

Belgorod State University, Belgorod, 308015, Russia

ABSTRACT

The effect of carbon content (x = 0, 0.5, and 2.0 at.%) on the phase composition, microstructure, and mechanical properties of thermomechanically processed CoCrFeMnNi system high-entropy alloys was studied. The molar fraction of Cr in the program $Co_1Cr_{0.25}Fe_1Mn_1Ni_1$ alloy was reduced to 0.25 compared with the equiatomic alloy to increase the solubility of carbon in the face-centred cubic solid solution. The as-cast alloys were cold rolled to 80% thickness reduction and then annealed at 600−1000 °C for 1 h. The addition of carbon to the CoCrFeMnNi alloys resulted in an increase in the temperature at which recrystallisation starts and in the precipitation of the Cr-rich $M_{23}C_6$ carbide particles. The volume fraction of the second phase increased with an increase in the carbon content and decreased with increasing annealing temperature. The formation of precipitates in the carbon-doped alloys strongly limited the matrix grain growth owing to the pinning effect. The thermomechanical processing of the alloys resulted in a reasonable work-hardening capacity and, therefore, in rather high ultimate tensile strength and ductility. Increasing the carbon content led to a pronounced increase in strength and a weak decrease in the ductility of the CoCrFeMnNi alloys. After annealing at 800 °C, the yield strength of the alloys increased from 313 MPa to 636 MPa, whereas the total elongation decreased from 56% to 43% with an increase in the carbon percentage from 0 at.% to 2.0 at.%. Decreasing the testing temperature to 77 K led to a simultaneous increase in both strength and ductility of the alloys. The alloy with 2.0 at.% of carbon demonstrated an attractive combination of mechanical properties at cryogenic temperature, presenting a yield and ultimate tensile strength of 786 MPa and 1218 MPa, respectively, along with a ductility of 52%. The effect of the carbon content on the microstructure development and strengthening mechanisms was discussed.

© 2020 Elsevier B.V. All rights reserved.

1. Introduction

The so-called high-entropy alloys (HEAs) have become a topic of great interest in materials science over the past few years [1,2]. It is believed that HEAs containing multiple principal elements (usually more than five) in close to equiatomic concentrations (5−35 at.%) may be preferable to conventional alloys based on a single element as the former present opportunities for attaining unique metal structures and properties [3−6]. Many of the introduced such alloys have demonstrated attractive properties, for example, capability of withstanding high temperatures [7−9].

High-entropy alloys based on 3d transition elements are the most studied among the HEA classes [2,10]. One representative example is the Cantor equiatomic CoCrFeMnNi alloy with a face-centred cubic (fcc) structure [11] that has high ductility and extremely high toughness at room temperature, which increases even further at cryogenic temperatures [12−15]. The properties of the alloy can be further improved by the proper selection of the alloying elements, for example, in the case of the CoCrNi equiatomic alloy, which has improved cryogenic strength and fracture toughness compared with the Cantor alloy [16−18]. However, CoCrFeMnNi-based alloys generally have rather low yield strength at room temperature [10,12,13,19].

One of the most effective ways to increase the strength of 3d transition metal-based HEAs involves the addition of interstitial elements [20−32]. A variety of elements can be used, for example, nitrogen or boron [33−37], but the most explored option is the addition of carbon. It is already well established that interstitial alloying can provide a significant increase in strength without

* Corresponding author. Laboratory of Bulk Nanostructured Materials, Belgorod State University, Pobeda 85, Belgorod, 308015, Russia.
   E-mail address: klimova_mv@bsu.edu.ru (M. Klimova).

compromising ductility. The carbon-doped HEAs can benefit from both solid solution strengthening due to the dissolved carbon atoms and precipitation strengthening due to the carbide formation [20,22,27−31,38−40]. The solid solution strengthening effect is quite straightforward—the strength increment is proportional to the content of the dissolved element(s). In the case of carbon in fcc HEAs, most studies have reported direct proportionality (or a linear relationship) [20,27,41]. The exact values of the carbon-caused solid solution strengthening effect, described in different sources, vary significantly, most probably due to differences in the matrix chemistry and the resulting lattice distortions by carbon atoms [24]. Note that solid solution strengthening can be particularly effective at cryogenic temperatures [41].

However, solid solution strengthening has obvious limitations owing to the limited solubility of carbon in the fcc matrix. Thus, special alloy designing and/or processing are required to obtain a sufficiently high amount of carbon in the solid solution. Meanwhile, another effective strengthening mechanism is associated with grain-boundary hardening due to the high Hall−Petch coefficient characteristic of fcc HEAs [12]. Conventional thermomechanical processing comprising cold working and subsequent annealing can be effectively used for this purpose. In addition to recrystallisation of the fcc matrix, such processing of carbon-doped HEAs can most probably result in the precipitation of carbide particles, as shown in numerous publications [21,25,28,31,38,40,42−44]. However, despite the many studies regarding the thermomechanical processing of carbon-doped alloys, a complete understanding of the microstructure and mechanical properties of these alloys remains deficient. It was recently demonstrated that second-phase precipitates could strongly impede grain growth, resulting in the formation of an ultrafine-grained recrystallised fcc microstructure [38,45]. Such dual-phase precipitation-hardened structures can be expected to possess enhanced mechanical properties. However, the optimal chemical compositions of the alloys and processing conditions for obtaining proper microstructures are unclear. In addition, very limited information regarding the cryogenic mechanical behaviour of such alloys is, as yet, available in the literature [46,47].

Therefore, CoCrFeMnNi high-entropy alloys with different carbon contents (x = 0, 0.5, and 2.0 at.%), introduced in a previous work [41], were cold rolled and annealed at different temperatures in the range of 600−1000 °C to study the structure and mechanical properties at room and cryogenic temperatures. Links between chemistry, processing conditions, microstructure, and mechanical properties were established.

2. Materials and methods

Carbon-containing high-entropy alloys with non-equiatomic concentrations of the principal elements ($Co_1Cr_{0.25}Fe_1Mn_1Ni_1$ in the molar ratio) and different amounts of carbon (the nominal concentrations were 0, 0.5, and 2.0 at.%) were produced by vacuum induction melting. The measured chemical composition of alloys was close to the nominal composition (see Table 1 and [41]). The as-cast alloy samples were cold rolled at room temperature to a

Table 1
Chemical composition of the program alloys depending on the carbon concentration, in at.%.

Nominal carbon content, at.%	Concentration of the elements, at.%					
	Co	Cr	Fe	Mn	Ni	C
x = 0	23.29	6.22	23.90	23.09	23.46	0.03
x = 0.5	23.17	6.42	23.97	23.67	22.24	0.53
x = 2.0	23.42	6.23	22.41	22.02	23.82	2.11

thickness reduction ratio of 80% (from 8.0 to 1.6 mm). Then, the samples were annealed in a muffle furnace in an air atmosphere at temperatures of 600−1000 °C for 1 h followed by air cooling.

The structure of the alloy was studied using X-ray diffraction (XRD) analysis, scanning (SEM), and transmission (TEM) electron microscopy in the RD−ND plane (perpendicular to the transversal direction). XRD analysis was performed using a RIGAKU diffractometer with Cu Kα irradiation. SEM studies were carried out using an FEI Quanta 600 FEG microscope equipped with a backscattered electron (BSE) detector. Samples for SEM observations were mechanically polished with different SiC papers and a colloidal silica suspension. TEM investigations were conducted using a JEOL JEM-2100 microscope with an accelerating voltage of 200 kV equipped with an energy dispersive spectrometry (EDS) detector. Selected area electron diffraction (SAED) patterns were used for the phase identification and results of EDS for chemical analysis. Samples for TEM analysis were prepared by conventional twin-jet electro-polishing of mechanically pre-thinned 100 μm foils in a mixture of 90% CH_3COOH and 10% $HClO_4$ at a potential of 30 V at room temperature. The size/fractions of recrystallised grains and the size/number of precipitates were quantified using at least 10 SEM or TEM images at low magnification.

An equilibrium phase diagram was constructed using Thermo-Calc (version 2020a) software with a high-entropy alloy TCHEA3 database.

Vickers microhardness tests were conducted at room temperature using a 300 g load. At least 20 measurements per data point were made. Tensile tests at room (293 K) and cryogenic (77 K) temperatures of dog-bone flat specimens (gauge measured $6 \times 3 \times 1.5$ mm^3) were conducted using an Instron 5882 universal testing machine at a constant crosshead velocity corresponding to a nominal strain rate of 10^{-3} s^{-1}. For cryogenic testing, the test specimen and both grips were held in an open-top vessel filled with liquid nitrogen before the test started to equilibrate the temperature. Elongation to fracture was determined by measuring the spacing between marks designating the gauge length before and after the test. Some tests were repeated using the VIC-3D system; the obtained results were consistent with the data obtained during testing without the extensometer. At least three specimens of each composition and temperature were tested.

3. Results

3.1. Microhardness

The dependence of the microhardness of the program alloys on the annealing temperature is shown in Fig. 1. The annealing time
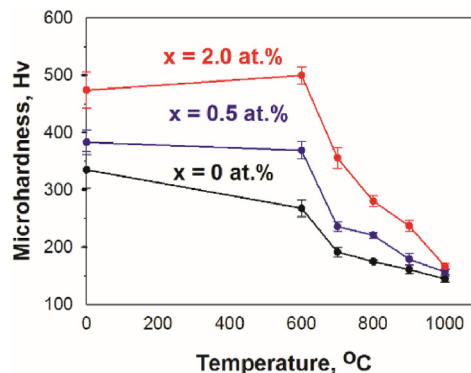
Fig. 1. Effect of annealing temperature on the microhardness of the CoCrFeMnNi alloys with different carbon contents (x): x = 0, 0.5, 2.0 at.%.

was 1 h. In the cold-rolled condition, the hardness gradually increased with an increase in the carbon content. Annealing at 600 °C resulted in a decrease in the hardness of the alloy with x = 0 at.%, while the two other alloys (with x = 0.5 at.% and x = 2.0 at.%) did not show noticeable changes in hardness. An increase in the annealing temperature to 700 °C resulted in a decrease in the hardness of all the carbon-doped alloys. At higher temperatures, the hardness decreased in the alloys at a lower rate. The microhardness of the alloys after annealing at 600−900 °C increased with increasing carbon content; however, annealing at 1000 °C resulted in similar microhardness values. A drastic softening in the temperature range of 600−800 °C was most probably associated with primary recrystallisation, which could readily develop in the cold-rolled samples.

3.2. Microstructure

All the CoCrFeMnNi alloys with different carbon contents after cold rolling to 80% thickness reduction had a lamellar-type microstructure mostly aligned with the rolling direction, consisting of twinned and (sub)grained areas (Fig. 2). It is worth noting that noticeable qualitative differences in the structures of alloys with different amounts of carbon were not observed. The presence of second-phase particles was not detected. The high density of twins and dislocations after rolling obviously resulted in the high hardness of the alloys (Fig. 1), while the observed difference in the hardness can be mostly attributed to the solid solution hardening, similar to that in the as-cast condition [41].

The effect of annealing at 700−1000 °C for 1 h on the microstructures of the cold-rolled CoCrFeMnNi alloys is illustrated in Fig. 3. Neither of the carbon-doped alloys annealed at 600 °C (not shown) showed any noticeable signs of recrystallisation. However, in the carbon-free alloy (x = 0 at.%), a partially recrystallised structure with the recrystallised fraction of 0.36 and a recrystallised grain size of 2.7 μm was observed (Fig. 3a). A higher magnification insert in Fig. 3a illustrates the absence of any secondary phases in recrystallised areas. A completely recrystallised structure was formed in the carbon-free CoCrFeMnNi alloy after annealing at 700 °C (Fig. 3b). Further increases in the annealing temperature led to the development of recrystallisation via the normal grain growth mechanism (Fig. 3e,h,k). Numerous annealing twins were observed inside the recrystallised grains.

The addition of carbon noticeably increased the temperature at which recrystallisation began. Only partial recrystallisation was observed in the carbon-doped alloys after annealing at 700 °C (Fig. 3c and d). The recrystallised fraction was approximately 0.93 and 0.68 in alloys containing 0.5 at.% and 2.0 at.% of carbon, respectively. The corresponding microstructures consisted of deformed areas and equiaxed recrystallised grains with a high density of annealing twins. Full recrystallisation of the carbon-doped alloys occurred only after annealing at 800 °C (Fig. 3f and g). The presence of numerous dark dots in the recrystallised carbon-doped alloys is most likely associated with carbide particles (see below). An increase in the annealing temperature to 900 °C and 1000 °C resulted in the coarsening of the recrystallised grains (Fig. 3i,j,l,m). Carbides were not found after annealing at 1000 °C (Fig. 3k−m).

The temperature dependence of the recrystallised grain size of the program alloys is shown in Fig. 4 and Table 2. The average recrystallised grain size of the carbon-free CoCrFeNiMn alloy gradually increased from 3.6 μm to 32.2 μm with an increase in the annealing temperature from 700 °C to 1000 °C. Addition of a small amount of carbon (0.5 at.%) resulted in only a moderate decrease in the recrystallised grain size. In turn, an increase in the carbon concentration to 2.0 at.% restricted the coarsening of the fcc grains considerably until 900 °C. However, the average grain size increased rapidly from 2.5 μm after annealing at 900 °C to approximately 25 μm after annealing at 1000 °C.

To obtain more details regarding the structure of the carbon-doped alloys, and in particular, to obtain more information regarding the precipitated particles, XRD analysis and TEM investigations of the annealed alloys were performed. Typical XRD curves (Fig. 5) of the carbon-doped alloys revealed that the crystal structures of the particles were $M_{23}C_6$-type carbides. At the same time, the annealed structures of the carbon-free alloy consisted of the fcc matrix phase, without any secondary phases.

TEM images of alloys with 0.5 at.% and 2.0 at.% carbon are presented in Figs. 6 and 7, respectively. The SAED patterns (inserts in Figs. 6 and 7) and EDS chemical analysis (Fig. 7i) also confirmed that the particles were $M_{23}C_6$-type carbides, which are mostly composed of Cr. The typical chemical compositions of the matrix and particles are given in Table 2. Because of the insufficient energy resolution of the TEM-EDS system used, only metallic elements were analysed. The sizes of the carbide particles and their volume fractions are summarised in Table 3. Note that no precipitates were detected in the carbon-free alloy after annealing at 600−1000 °C or in the carbon-doped alloys after annealing at 1000 °C.

Even a small amount of carbon (0.5 at.%) resulted in the precipitation of carbide particles at temperatures of 600−900 °C (Fig. 6). However, the amount of carbides was rather low (Fig. 6; Table 3). As shown in Fig. 6a, annealing at 600 °C was accompanied by recovery of the fcc matrix. In addition, some fine particles were
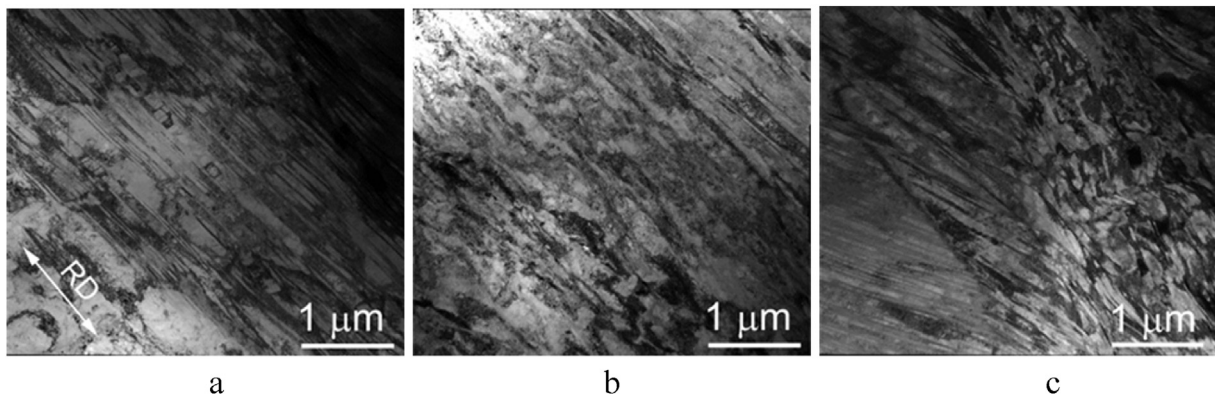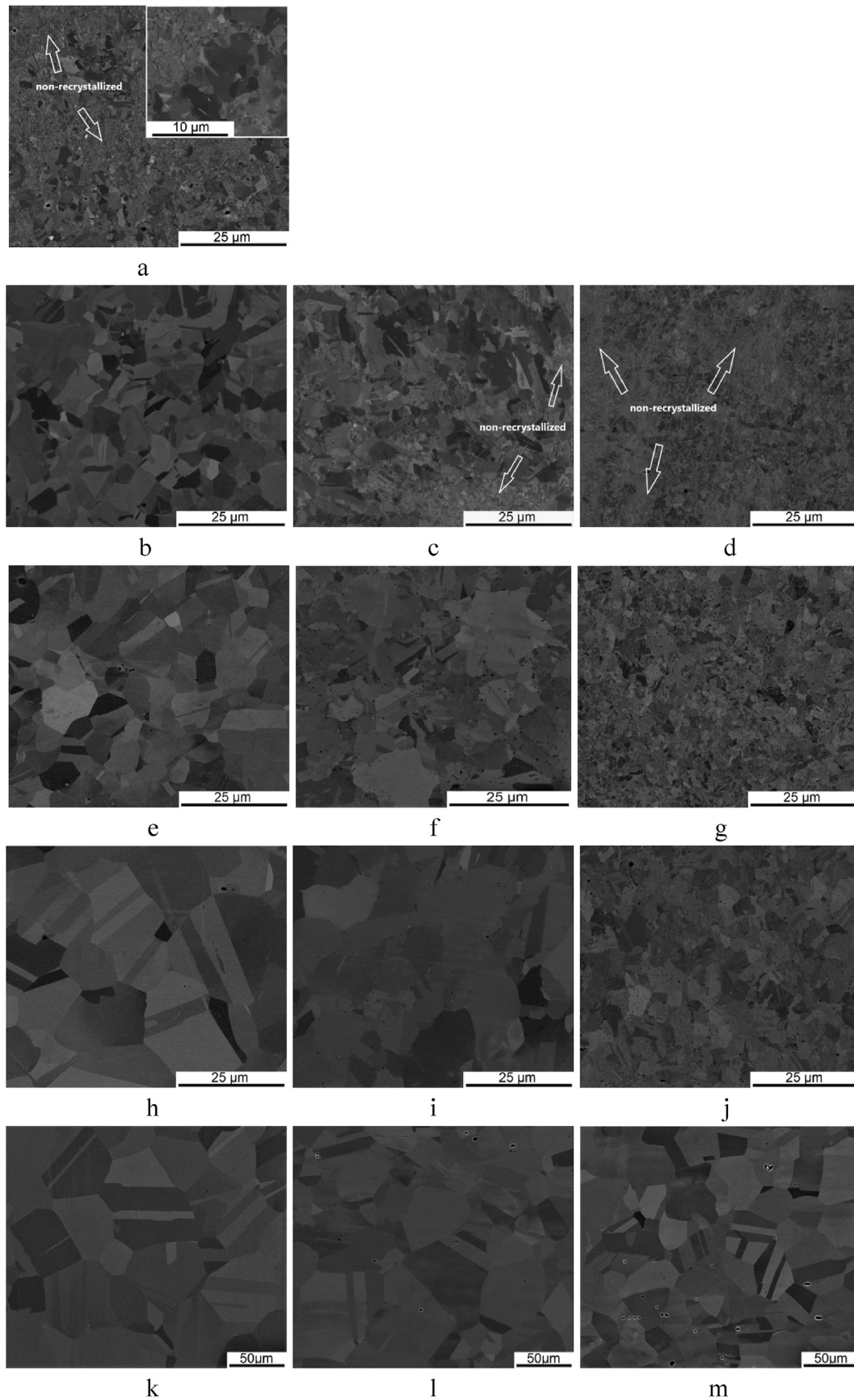

Fig. 2. Microstructure of the CoCrFeMnNi alloys with different carbon contents (x): x = 0 at.% (a); 0.5 at.% (b); 2.0 at.% (c) after cold rolling to 80% thickness reduction; TEM bright-field images.

Fig. 3. SEM-BSE images of the microstructure of the CoCrFeNiMn alloys with different carbon contents (x): x = 0 at.% (a,b,e,h,k); 0.5 at.% (c,f,i,l); 2.0 at.% (d,g,j,m) after annealing at 600 °C (a); 700 °C (b–d); 800 °C (e–g); 900 °C (h–j); 1000 °C (k–m).
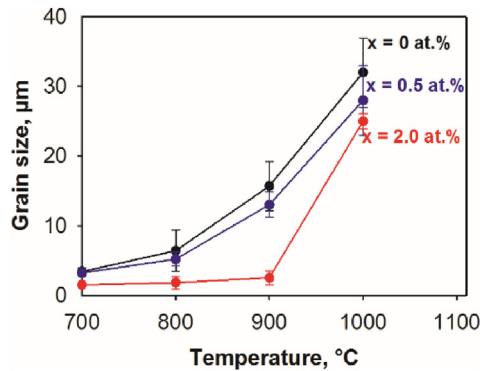
Fig. 4. Dependence of the recrystallised grain size on annealing temperature in the CoCrFeMnNi alloys with different carbon contents (x): x = 0, 0.5, 2.0 at.%.

Table 2
Chemical composition of the constitutive phases in the CoCrFeMnNi alloy with different carbon contents (x): x = 0.5, 2,0 at.% after cold rolling and annealing at 800 °C.

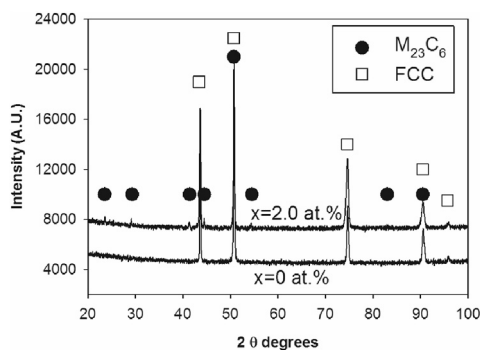| Elements, at.%	Co	Cr	Fe	Mn	Ni
x = 0.5 at.%					
Fcc matrix	23.4 ± 1	6.5 ± 1	26.3 ± 1	21.8 ± 2	22.0 ± 1
$M_{23}C_6$ particles	14.3 ± 3	34.3 ± 10	19.9 ± 2	18.8 ± 2	12.7 ± 4
x = 2.0 at.%					
Fcc matrix	23.4 ± 1	6.0 ± 1	25.3 ± 1	24.1 ± 1	21.2 ± 1
$M_{23}C_6$ particles	9.4 ± 3	47.1 ± 14	15.9 ± 3	20.9 ± 1	6.7 ± 2

Fig. 5. XRD patterns of the CoCrFeMnNi alloys with different carbon contents (x): x = 0, 2.0 at.% after cold rolling and annealing at 800 °C.

found in the recovered structure (insert in Fig. 6a). The size of the carbides gradually increased with annealing temperature; meanwhile, their fraction reached a maximum after annealing at 700 °C and then decreased (Fig. 6b, Table 3). The spatial distribution of the carbides was rather inhomogeneous; some grains or areas inside individual grains had a much higher density of the particles than the surroundings. In addition, carbides were quite often found at the grain boundaries. The grain-boundary precipitates were generally coarser than the intragranular precipitates.

An increase in the carbon concentration to 2.0 at.% did not result in qualitative changes in microstructure; however, the fraction of carbides was considerably higher (Fig. 7, Table 3). Annealing at 600°C did not lead to a noticeable development of the recrystallisation process (Fig. 7a). The lower part of the TEM image in Fig. 7a shows a typical deformed microstructure (compare with Fig. 2), whereas the upper part most likely corresponds to recovered areas with still noticeable dislocation density. A larger magnification

image from the same area (Fig. 7b) with the corresponding SAED pattern (Fig. 7c) revealed that the formation of new small grains and precipitation of tiny carbides occurred simultaneously. In addition, SAED suggests that the orientation relationship between the fcc matrix and the carbides was close to $(111)_{fcc} // (111)_{M23C6}$.

A partially recrystallised structure consisting of recovered regions and recrystallised (sub)grains was formed after annealing at 700 °C (Fig. 7d). It is worth noting that carbide particles were found both in the recovered (Fig. 7e) and recrystallised areas (Fig. 7f). The particles in the recovered areas were smaller than those observed both inside and at the boundaries of the recrystallised grains. In addition, the amount of the particles was much higher in the recrystallised areas; ~9% vs. 5.6% of the carbides in the whole volume.

An increase in the annealing temperature to 800 °C resulted in a noticeably higher fraction of the carbides distributed rather homogeneously in a fully recrystallised fcc matrix (Fig. 7g, Table 3). A further increase in the annealing temperature to 900 °C resulted in a decrease in the volume fraction of the particles, while their size continuously increased (Fig. 7h, Table 3). For example, the volume fraction of carbides decreased from 7.4% to 3.5% after annealing at 800 °C and 900 °C, respectively. In contrast, the particles rapidly grew from 77 nm to 200 nm with an increase in temperature from 700 °C to 900 °C.

3.3. Tensile properties

A series of tensile stress—strain curves obtained at room temperature for the CoCrFeMnNi alloys with different carbon contents after cold rolling and annealing at various temperatures are shown in Fig. 8. The representative mechanical properties, that is, yield strength (YS), ultimate tensile strength (UTS), total (TE), and uniform (UE) elongation, are summarised in Table 4. Qualitatively, the alloys exhibited rather similar behaviour. Cold-rolled samples demonstrated high YS with a short strain-hardening stage and early necking, resulting in low ductility. In addition, the strength of the cold-rolled alloys increased in proportion to the carbon content. For example, the YS of rolled specimens increased from 983 MPa to 1485 MPa with an increase in the carbon percentage from 0 at.% to 2.0 at.%.

Annealing after rolling resulted in softening and enhancement of the ductility of the alloys. After annealing at 700 °C, the most pronounced softening was observed in the undoped alloy; the YS decreased by 2.5 times to 387 MPa (Fig. 8a). With an increase in the annealing temperature, the strength of the alloy gradually decreased to 207 MPa. The annealed alloy exhibited reasonable work-hardening capacity and, therefore, a rather high UTS and ductility. The elongation to fracture, however, increased moderately from 53% to 60% as the annealing temperature changed from 700°C to 1000 °C.

The YS of the alloy doped with 0.5 at.% of carbon was ~50−70 MPa higher than that of the undoped alloy after annealing at the same temperatures (Fig. 8b). The only exception was found after annealing at 700 °C. In this case, the carbon-doped alloy was ~1.5 times stronger. A further increase in the annealing temperature to 800 °C resulted in a pronounced decrease in the YS to 380 MPa, most probably due to complete recrystallisation. The softening was accompanied by an increase in ductility from 42% to 52% after annealing at 700 °C and 800 °C, respectively. Further increases in the annealing temperature resulted in a gradual decrease in strength and an increase in ductility.

The alloy with the highest carbon percentage (2.0 at.%) showed a qualitatively similar response of the mechanical properties to recrystallisation annealing; however, this alloy was considerably stronger than the two other alloys (Fig. 8c). For example, the YS of
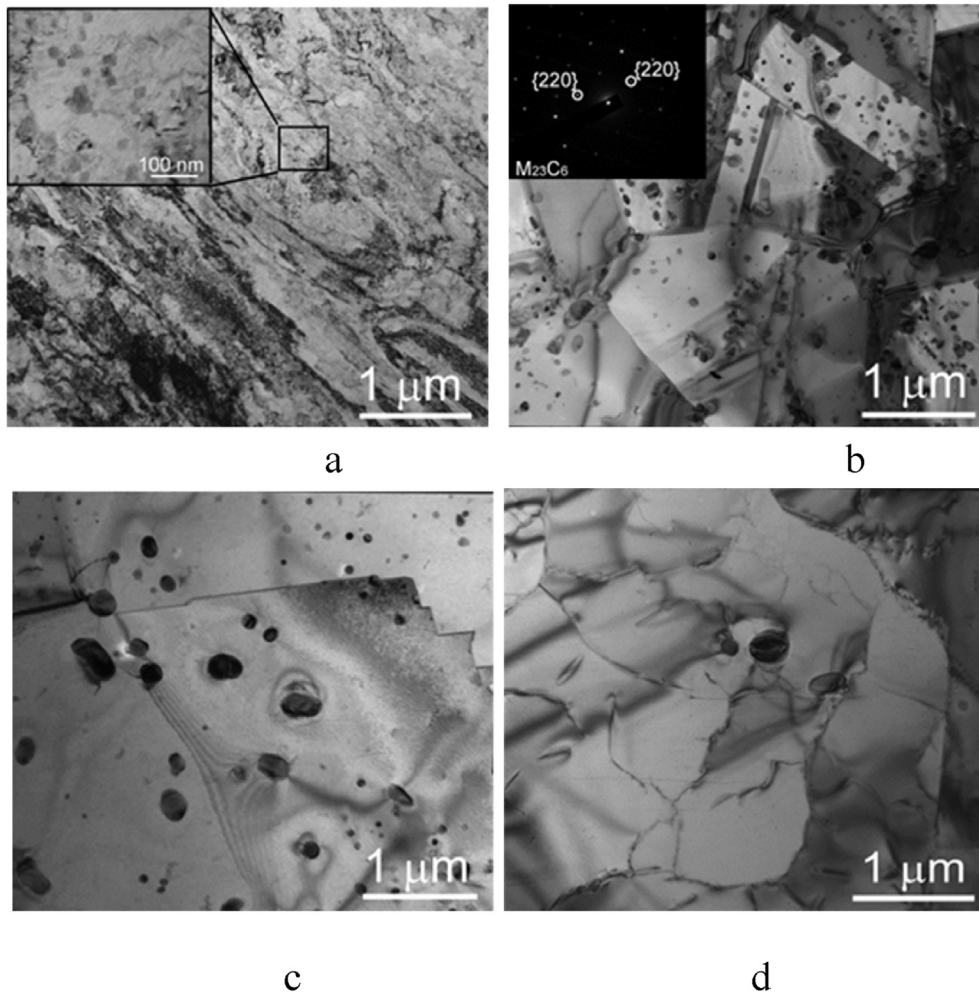
Fig. 6. TEM microstructure of the CoCrFeMnNi alloy with x = 0.5 at.% of carbon after annealing at 600 °C (a); 700 °C (b); 800 °C (c); 900 °C (d).

the x = 2.0 alloy decreased from 860 MPa to 635 MPa after annealing at 700 °C or 800 °C, respectively, and then decreased gradually to 380 MPa after annealing at 1000 °C (Fig. 7c). In addition, note the sharp yield point on the stress—strain curves for the alloy annealed at 800 °C and 900 °C. The ductility of the alloy increased significantly from 24% to 55%, with an increase in the annealing temperature from 700 °C to 1000 °C. An increase in the carbon concentration from 0.5 at.% to 2.0 at.% resulted in lower ductility under all examined conditions.

Additional tests at liquid nitrogen temperature (77 K) were performed for the conditions that demonstrated an attractive balance of strength and ductility at room temperature (Fig. 9, Table 5). Decreasing the test temperature to 77 K led to a simultaneous increase in both strength and ductility of the alloys. Similar dependencies of mechanical properties on the carbon concentration were observed at 293 K and 77 K: the strength slightly increased as the carbon concentration increased from 0 at.% to 0.5 at.%, and then increased considerably when the carbon content approached 2.0 at.%. In turn, the highest ductility was obtained for the alloy with 0.5 at.%. Finally, an increase in the annealing temperature from 800 °C to 900 °C resulted in a decrease in the YS and higher ductility. However, the effect of annealing temperature decreased as the concentration of carbon increased.

The strain-hardening curves of the CoCrFeMnNi alloys with different carbon contents after annealing at 800 °C obtained during tension at room or cryogenic temperatures are shown in Fig. 10. The alloys demonstrated qualitatively similar behaviour irrespective of the carbon content or testing temperature. The strain-hardening rate of the alloys was maximum at the initial stages of deformation, and then decreased gradually until a rapid decrease occurred in the final stages of deformation. No inflexions were observed. The sharp decrease in the strain-hardening rate of the alloy with 2.0 at.% at the beginning of the deformation is associated with the sharp yield point (Fig. 8c). An increase in the amount of carbon leads to an increase in the strain hardening at the initial stages of deformation. However, after a true strain of ~0.2, the hardening rate became inversely proportional to the carbon content. In addition, the strain-hardening capacity of the alloys was found to be better at cryogenic temperatures. The strain-hardening curves for the other conditions are not shown because they exhibit qualitatively similar behaviour.

4. Discussion

The present study demonstrated that cold working followed by annealing at 600—1000 °C of the CoCrFeMnNi high-entropy alloys doped with different amounts of carbon resulted in (i) recrystallisation of the cold-worked fcc matrix and (ii) the precipitation of the $M_{23}C_6$-type carbides (Figs. 3, 5—7). The recrystallised alloys demonstrated attractive mechanical properties, that is, strength
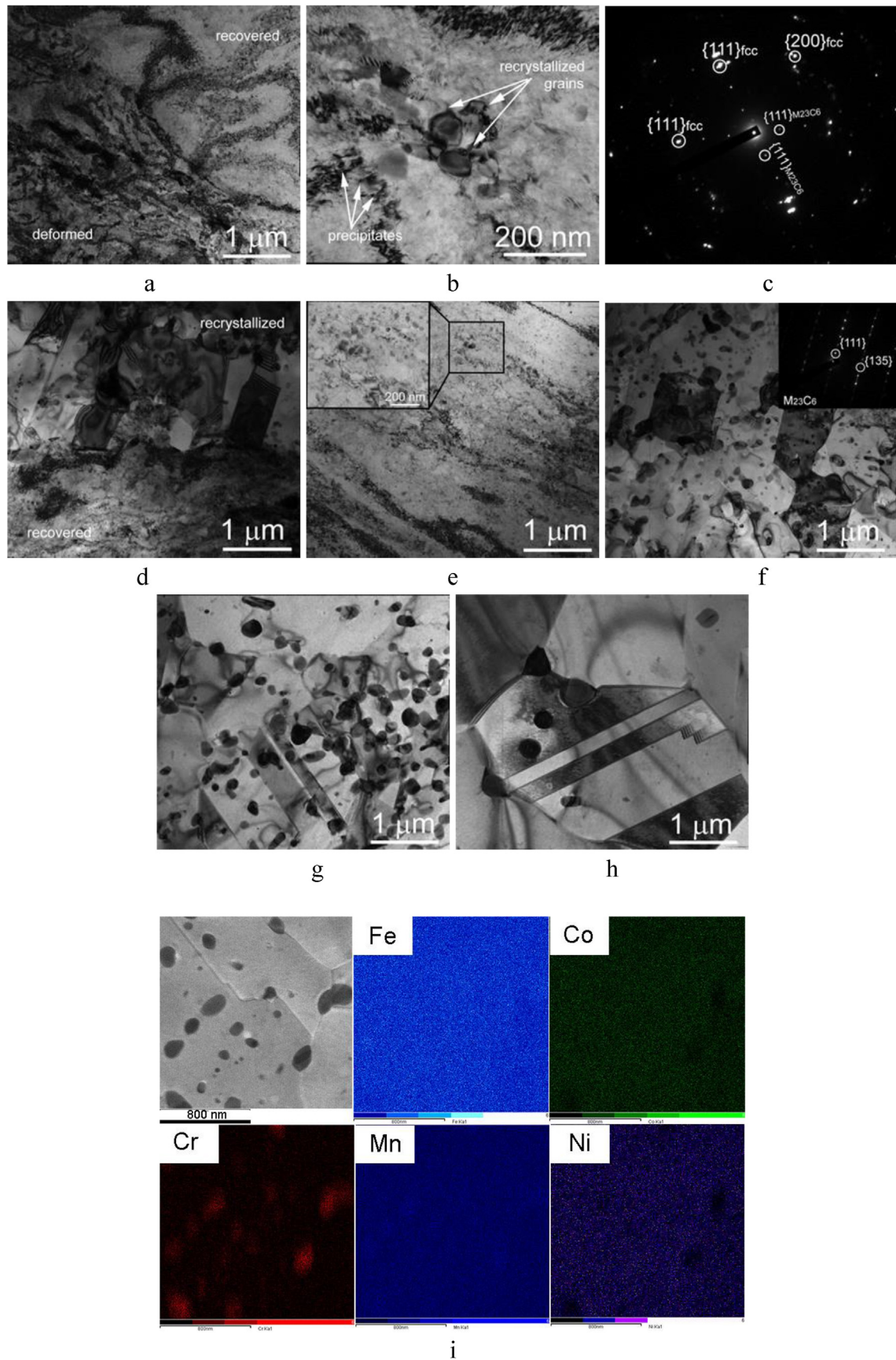
Fig. 7. TEM microstructure of the CoCrFeMnNi alloy with x = 2.0 at.% of carbon after annealing at 600 °C (a,b,c); 700 °C (d,e,f); 800 °C (g,i); 900 °C (h); bright-field images (a−h) and STEM image with corresponding EDX maps (i).

Table 3
Microstructure parameters of the CoCrFeMnNi alloys with different carbon contents (x): x = 0, 0.5, 2.0 at.% after cold rolling and annealing at temperatures of 700−1000 °C.

Annealing temperature °C	x = 0 at.%	x = 0.5 at.%			x = 2.0 at.%		
	Grain size, μm	Grain size, μm	Particle size, nm	Volume fraction, %	Grain size, μm	Particle size, nm	Volume fraction, %
700	3.6 ± 1.6	3.1 ± 1.8	63 ± 23	3.4/3.8[a]	1.4 ± 0.5	77 ± 20	5.6/8.9[a]
800	6.4 ± 2.9	5.2 ± 3.0	89 ± 20	1.5	1.6 ± 0.9	117 ± 70	7.4
900	15.7 ± 7.8	12.9 ± 3.6	165 ± 112	0.6	2.5 ± 1.0	203 ± 140	3.5
1000	32.2 ± 15.4	28.3 ± 14.0	−	−	25.1 ± 12.1	−	−

[a] The nominator and denominator correspond to the total fraction of the carbides and the fraction of the carbides in the recrystallised areas, respectively.
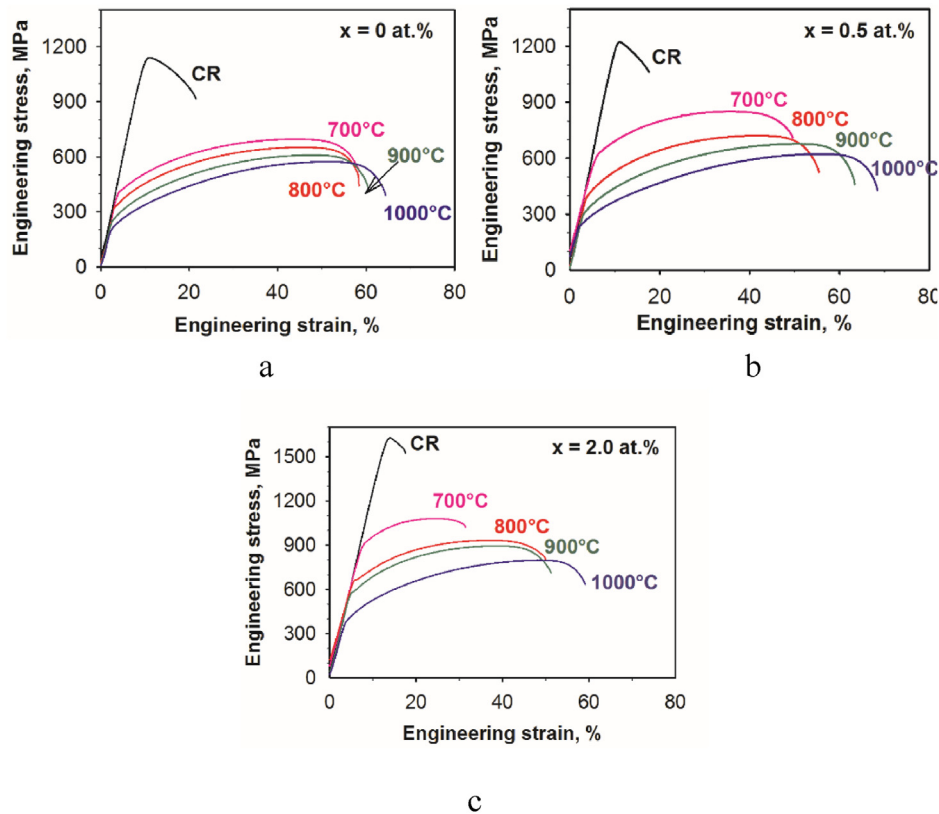
Fig. 8. Room temperature tensile stress-strain curves of the CoCrFeMnNi alloys with different carbon contents (x): x = 0 at.% (a); 0.5 at.% (b); 2.0 at.% (c) after cold rolling and annealing at different temperatures.

and ductility, both at ambient and cryogenic temperatures (Figs. 8 and 9). Moreover, it was found that the carbon content strongly affected both the microstructure development and mechanical properties after annealing. Several aspects of the carbon effect are analysed further.

The carbon-free alloy was found to have a single fcc phase microstructure in all the examined conditions (Figs. 2,3). Note that in the equiatomic CoCrFeMnNi alloy, different types of precipitates, including Cr-rich sigma and bcc phases, were found after cold rolling and annealing at 600−800 °C [45,48,49]. Presumably, the reduced Cr concentration (Table 1) could be responsible for the absence of any secondary phases in the program carbon-free alloy.

In turn, the most apparent effect of carbon addition was associated with the precipitation of Cr-rich $M_{23}C_6$ carbides. It is worth noting that no or very limited amounts of carbides were found in the as-cast microstructure of the same alloys [41], which is consistent with the observations recorded under the cold-rolled condition (Fig. 2). However, the amount of carbon solved in the fcc matrix of the as-cast alloys, according to the observations of the present study, appears to be much higher than the equilibrium solubility of carbon in fcc solid solution at temperatures ≤900 °C. As a result of the heat treatment, an excessive amount of carbon partitions to the carbide particles. The formation of the dual-phase microstructure, composed of the fcc matrix and carbide particles, agrees with the Thermo-Calc predictions. A comparison between the experimental fraction of carbides and the equilibrium fraction predicted using Thermo-Calc software is shown in Fig. 11. Note that the fraction of carbides in recrystallised areas was used in the case of annealing at 700 °C.

The comparison in Fig. 11 shows that the experimental carbide volume fractions are higher than the equilibrium fractions. However, the overall trend of a gradual decrease in the fraction of the carbides with an increase in the annealing temperature in both alloys was confirmed. This finding is associated with the higher solubility of carbon in the fcc matrix at higher temperatures. According to the Thermo-Calc predictions, the solvus temperature of the carbides varied significantly: the corresponding temperatures were 852 °C and 1042 °C at carbon concentrations of 0.5% and 2.0%,

Table 4
Room temperature mechanical properties of the CoCrFeMnNi alloys with different carbon contents (x): x = 0, 0.5, 2.0 at.% after cold rolling (CR) and annealing at different temperatures.

Condition	YS, MPa	US, MPa	TE, %	UE, %
x = 0 at%				
CR	983	1139	14	
700 °C	387	696	53	38
800 °C	313	651	56	41
900 °C	251	609	57	43
1000 °C	207	572	60	45
x = 0.5 at%				
CR	1119	1223	9	
700 °C	565	851	42	28
800 °C	381	721	52	36
900 °C	299	677	58	44
1000 °C	236	623	64	49
x = 2.0 at%				
CR	1485	1627	5	
700 °C	859	1081	24	15
800 °C	636	933	43	29
900 °C	562	895	46	32
1000 °C	380	797	55	42

respectively. However, the experimental data showed that in both alloys, carbides were found at 900 °C, while a single fcc phase structure was observed at 1000 °C. Fig. 11 suggests that the solvus temperatures were close to 900 and 1000 °C in the alloys with 0.5 at.% and 2.0 at.% of carbon, respectively. The discrepancies between the experimental data and calculations can be attributed to the well-known imperfections of the available databases [3].

The addition of carbon to the CoCrFeMnNi alloy led to an increase in the recrystallisation temperature. This effect appears to be associated with the presence of carbon in the solid solution rather than the precipitation of the carbides. Because of the strong interaction of interstitial solutes with grain boundaries and the formation of solute atmospheres, the migration of grain boundaries is impeded [50], which leads to a higher energy barrier for recovery and recrystallisation during annealing. A similar suggestion was made in Ref. [25]. Precipitation of the particles was observed to occur simultaneously with recrystallisation (Fig. 7a−c), most probably because of the mass transfer needed for the particle growth.

Another effect of carbon doping was associated with a lower recrystallised grain size, especially in the alloy with 2.0 at.% of

carbon, after annealing at temperatures ≤900 °C (Fig. 4). On the other hand, rapid grain growth in the carbon-doped alloys was observed at T = 1000 °C, that is, in the single fcc phase field. Most likely, the precipitation of carbides restricted the fcc matrix grain growth. This effect was obviously stronger in the alloy with higher carbon content. The limiting grain size due to the particle pinning effect can be expressed according to Zener's original consideration [50]:

$$D_Z = a \frac{2d}{3F_v} \tag{1}$$

where D_z is the Zener limiting grain size, α is a scaling factor, and d and F_v are the size and fraction of particles, respectively. The relationships between the experimental fcc grain size and particle size/fraction ratio in the alloys (Table 3) with 0.5 at.% and 2.0 at.% of carbon after annealing at 700−900 °C are plotted in Fig. 12.

Fig. 12 shows that the relationship between the fcc grain size and the particle size/fraction ratio for both alloys can be described by a linear function, thereby confirming that the fcc grain growth rate was controlled by the Zener drag mechanism. The estimated slopes of the lines were $\alpha = 0.5$ and $\alpha = 0.3$ for the alloys doped with 0.5 at.% and 2.0 at.%, respectively (Fig. 12). Obviously, in the alloy with 2.0 at.% of carbon, the grain growth occurred much slower, which is consistent with the higher fraction of carbides. The obtained values of α are similar to those found in Ref. [51,52] ($0.25 < \alpha < 0.5$) and are likely associated with the concurrent precipitation of particles and nucleation of grains, which is confirmed by the microstructure observations (Fig. 7).

The amount of carbon also affected the mechanical properties of the alloys (Figs. 8 and 9, Tables 4 and 5). The contribution of different strengthening mechanisms was further evaluated. Note that work hardening is not considered in detail because this study is mainly focussed on recrystallised microstructures and properties. In the carbon-free alloy after cold rolling and annealing at 700−1000 °C, the main contribution to hardening comes from the grain boundaries. The dependence of the YS on the grain size (Hall−Petch relationship) (shown in Fig. 13a) can be expressed as:

$$\sigma_{H\text{-}P} = \sigma_0 + k\,D^{-0.5} \tag{2}$$

where σ_0 is the friction stress, D is the average grain size, and k is a numerical factor.

Fig. 13a shows that a linear relationship has the following parameters: $\sigma_0 = 125$ MPa and $k = 494$ MPa/μm$^{0.5}$. The same σ_0 and k
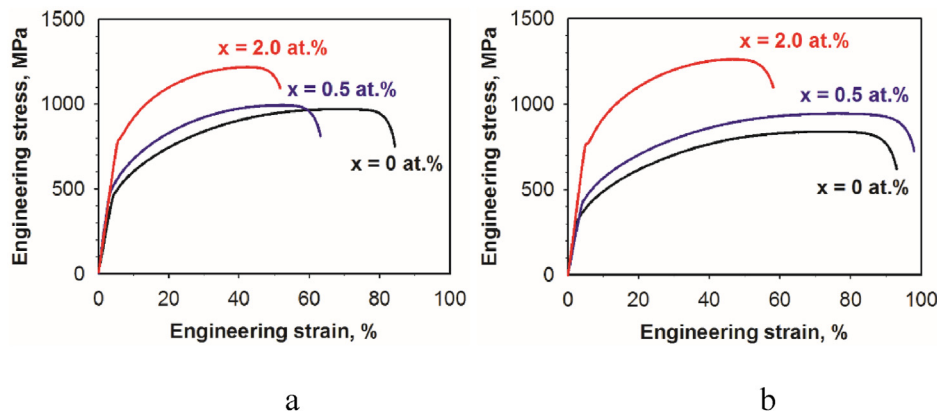
Fig. 9. Tensile stress-strain curves of the CoCrFeMnNi alloys with different carbon contents (x): x = 0, 0.5, 2.0 at.% after cold rolling and annealing at 800 °C (a) and 900 °C (b) obtained at cryogenic temperature.

Table 5
Mechanical properties of the CoCrFeMnNi alloys with different carbon contents (x): x = 0, 0.5, 2.0 at.% of after cold rolling and annealing at 800 °C and 900 °C obtained at cryogenic temperature.

Annealing temperature	YS, MPa	US, MPa	TE%	UE%
x = 0 at%				
800 °C	460	970	76	57
900 °C	310	838	87	64
x = 0.5 at%				
800 °C	480	994	62	48
900 °C	434	944	92	66
x = 2.0 at%				
800 °C	786	1218	52	39
900 °C	765	1262	56	42

Fig. 11. Dependence of the equilibrium carbides fraction predicted by Thermo-Calc software in comparison with the experimental data in the CoCrFeMnNi alloys with different carbon contents (x): x = 0.5, 2.0 at.%.
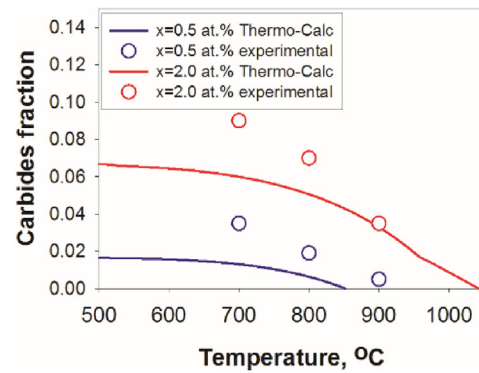
values have been previously reported for the equiatomic single-phase CoCrFeMnNi high-entropy alloy [12]. However, similar processing can result in noticeably higher strength in the equiatomic CoCrFeMnNi alloy. For example, the equiatomic alloy after cold rolling and subsequent annealing at 700 °C had a YS of 585 MPa [45], while the program alloy with reduced Cr content had a strength of only 387 MPa (Table 4). The lower strength of the program alloy can be attributed to the absence of secondary phases in the microstructure.

Thus, it seems reasonable that the precipitation of carbides also increases the strength of the carbon-doped alloys. The effect of precipitates on the strength via the Orowan mechanism can be considered using the following equation [53]:

$$\sigma_{Or} = (0.538\ G\ b\ f^{1/2}\ /\ d)\ ln\ (d/2b), \tag{3}$$

where $b = 2.58 \times 10^{-10}$ m^{-10} is the Burgers vector, $G = 80$ GPa is the shear modulus [10], and f and d are the particle fraction and size (Table 3), respectively.

The comparison between the experimental YS and calculated values using equations (2) and (3) is presented in Fig. 13b and c, and Table 6. Good agreement was found for the alloy with x = 0.5 at.% carbon (Fig. 13b), while some discrepancies were found for the alloy with 2.0 at.% of carbon (Fig. 13c). Some reasons for these discrepancies were further analysed. Meanwhile, both alloys demonstrated a steady decrease in both grain boundaries and precipitation strengthening with an increase in annealing temperature. Apparently, this is due to the coarsening of both grains and carbide particles. Moreover, it should be noted that the highest increment in strength for both alloys was provided by grain

refinement after thermomechanical processing. However, the fine grain size in the alloy with 2.0 at.% of carbon is also due to carbides precipitation (Fig. 12), that is, the strength of the alloy comes from carbides but in an indirect way [45,54,55].

The calculated and experimental YSs of the 2.0 at.% carbon alloy are noticeably unmatched after annealing at 700 °C or 1000 °C. In the former case, the experimental strength was remarkably higher than the calculated value. This difference can be associated with only partial recrystallisation of the alloy after annealing at 700 °C and a rather high amount of non-recrystallised fraction with a high density of defects (0.32) (Fig. 3). However, due to recovery development in the unrecrystallised areas (Fig. 7c), it is impossible to quantify the contribution from these areas, as in Refs. [38,45]. Note also that in the alloy with 0.5 at.%, the amount of non-recrystallised areas was only 0.07 and, therefore, they did not have a noticeable influence on the mechanical properties of the alloy.

After annealing at 1000 °C, the experimental YS of the alloy was also much higher than the predicted YS. In this case, the alloy has a single fcc phase solid solution structure, that is, the carbon atoms are fully solved in the matrix in contrast to the lower temperature annealing when carbon preferably partitions to the carbide particles. Therefore, much stronger solid solution strengthening is expected. The difference between the experimental and calculated YS of approximately 150 MPa at 1000 °C is consistent with solid solution strengthening, which was previously defined in Refs. [41] as 67 MPa/at% of carbon. Again, in the alloy with 0.5 at.% of carbon, this effect is negligible.
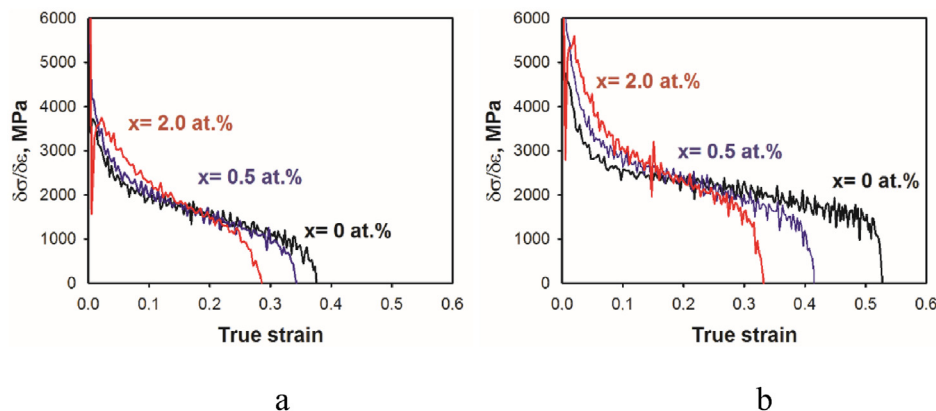
Fig. 10. Strain hardening curves of the CoCrFeMnNi alloys with different carbon contents (x): x = 0, 0.5, 2.0 at.% after cold rolling and annealing at 800 °C obtained at room (a) and cryogenic (b) temperature.
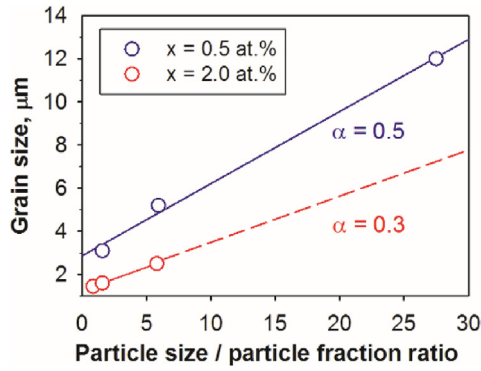
Fig. 12. Dependence of the fcc grain size on the particles size/fraction ratio in the CoCrFeMnNi alloys with different carbon contents (x): x = 0.5, 2.0 at.%. The dashed lines are only guides to eyes.

The ductility of the alloys decreased with increasing carbon content, which is consistent with previous studies [25,28,41]. Deformation mechanisms in fcc metals and alloys are strongly dependent on the stacking fault energy (SFE) value [56]. The TWIP (twinning-induced plasticity) or TRIP (transformation-induced plasticity) effects, which provide high ductility and strain-hardening capacity, are expected in alloys with low SFE. In interstitial HEAs, the addition of carbon can result in an increase in SFE and, therefore, in the suppression of mechanical twinning [25,26,57]. The shape of the strain-hardening curves (Fig. 10) suggests dislocation-mediated microband-induced plasticity with no or weak contribution of mechanical twinning [58]. These observations agree reasonably with the earlier results regarding the deformation mechanisms of the same alloys in the as-cast condition [41]. The presence of deformation twins in the heavily cold-worked alloys (Fig. 2) can be attributed to higher plastic strain and stresses as well as other differences in deformation conditions.

Another simple method to estimate the strain-hardening capacity is to use the difference between the UTS and YS [31,32]. The dependence between the uniform elongation and UTS-YS values of the CoCrFeMnNi alloys with different carbon contents is shown in Fig. 14. The ductility of the alloys increased with an increase in the work-hardening capacity. However, it appears that at nearly the same UTS-YS values, the elongation was inversely proportional to the carbon content (see dots highlighted with the oval in Fig. 14). That is, despite similar work-hardening capacity, ductility becomes lower in the alloys with higher carbon content. A similar behaviour was reported in Ref. [31] with respect to the equiatomic CoCrFeMnNi and CoCrFeMnNi-1at.%C alloys. This effect can be potentially attributed to the negative effect of hard carbide particles; the carbide/matrix interphases can serve as preferred places for crack initiation. However, the alloys examined in Ref. [31] had a single fcc phase structure. Thus, additional studies are required to understand the effect of carbon on the ductility of CoCrFeMnNi-based alloys because it is beyond the scope of the current paper.

Finally, a decrease in the tensile deformation temperature from 293 K to 77 K led to the simultaneous enhancement of strength and ductility of the alloys (Fig. 9). It is known that a decrease in temperature results in lower SFE values, thereby enhancing work-hardening capacity due to the activation of TWIP/TRIP effects [23,56,59]. However, the program alloys in the as-cast condition did not show any signs of mechanical twinning after tension to $\varepsilon = 20\%$ even at cryogenic temperatures [41], in contrast to the equiatomic CoCrFeMnNi alloy where development of twinning was observed after 7.4% strain [60]. Improvements in the mechanical properties of

$$YS = 125(MPa) + 0.494(MPa \cdot \mu m^{0.5}) D^{-0.5}$$

a

b

c
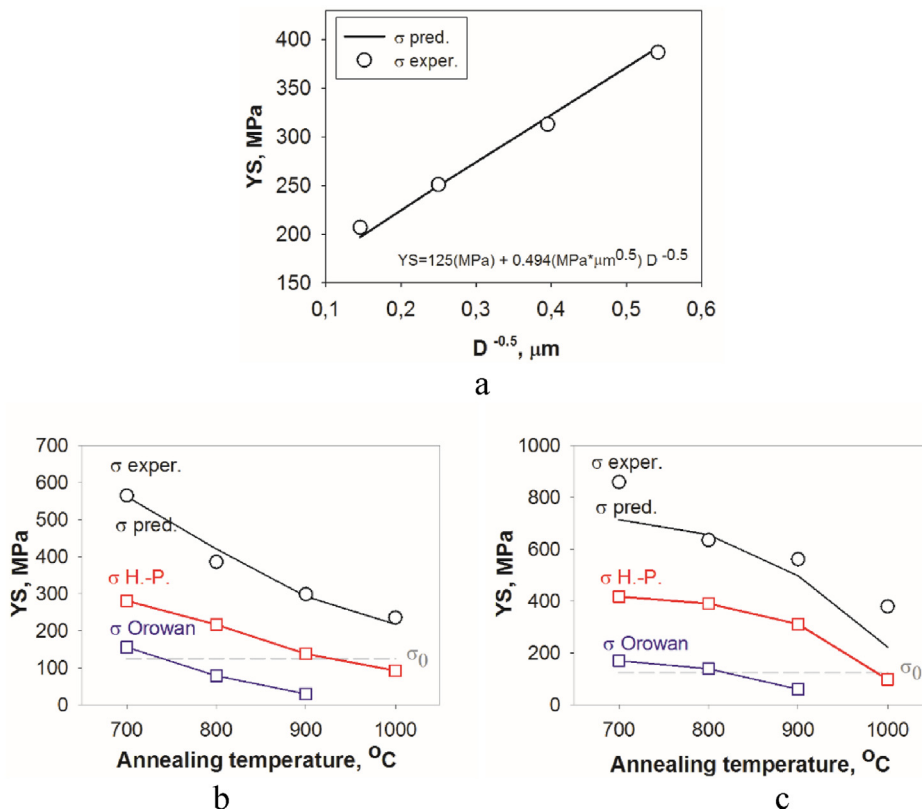
Fig. 13. Yield strength of the CoCrFeMnNi alloys with different carbon contents (x): x = 0 at.% (a); 0.5 at.% (b); 2.0 at.% (c) depending on grain size (a) or annealing temperature (b,c).

Table 6
Contributions of different strengthening mechanisms of the CoCrFeMnNi alloys with different carbon contents (x): x = 0.5, 2.0 at.% after cold rolling and annealing at different temperatures.

Annealing temperature	σ_0	$\sigma_{H.-P.}$	σ_{Orowan}	$\sigma_{pred.}$	$\sigma_{exper.}$
x = 0.5 at%					
700 °C	125	281	156	562	565
800 °C	125	217	79	421	381
900 °C	125	138	30	293	299
1000 °C	125	93	–	218	236
x = 2.0 at%					
700 °C	125	418	171	714	859
800 °C	125	391	140	656	636
900 °C	125	312	61	498	562
1000 °C	125	99	–	224	380
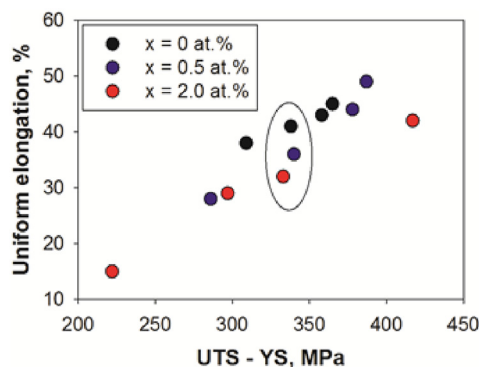
Fig. 14. The relationship between the ultimate tensile strength and yield strength difference and uniform elongation values in the CoCrFeMnNi alloys with different carbon contents (x): x = 0, 0.5, 2.0 at.%.

the program alloys in the as-cast condition were associated with the intensification of planar dislocation slip [41,61]. It is likely that similar mechanisms are also responsible for the strength and ductility enhancement in the examined thermomechanically processed alloys.

5. Conclusions

In this work, the phase composition, microstructure, and mechanical properties at ambient and cryogenic temperatures of CoCrFeMnNi high-entropy alloys doped with different amounts of carbon (0, 0.5, or 2.0 at.%) after cold rolling and annealing at 600−1000 °C were studied. The following conclusions were drawn:

1) After cold rolling, the alloys had typical cold-worked lamellar microstructures; the carbon content did not have a noticeable influence on the structure development. Annealing resulted in (i) recovery and/or recrystallisation of the fcc matrix and (ii) precipitation of Cr-rich $M_{23}C_6$ carbides in the carbon-doped alloys at 600−900 °C. The recrystallisation temperature was higher in the carbon-doped alloys, and recrystallisation and carbide precipitation mostly occurred concurrently. The volume fraction of carbides increased with an increase in the carbon content and decreased with increasing annealing temperature, which is in reasonable agreement with the equilibrium fraction of carbides predicted by Thermo-Calc.

2) The fcc grain growth in the carbon-doped alloys was inhibited by the carbide particles owing to the Zener drag mechanism. For example, the average grain size of the carbon-free CoCrFeNiMn

alloy gradually increased from 3.6 μm to 15.7 μm after annealing at 700 °C and 900 °C, whereas in the alloy with 2 at.% of carbon, the respective grain size varied from 1.4 μm to 2.5 μm. Rapid grain growth was observed in the carbon-doped alloys after annealing at 1000 °C, that is, in the single fcc phase field.

3) An increase in the carbon content resulted in a noticeably higher strength of the CoCrFeMnNi alloys. For example, after cold rolling and annealing at 800 °C, the yield strength at room temperature increased from 313 MPa to 636 MPa with an increase in the carbon percentage from 0 at.% to 2.0 at.%. Grain refinement provided a substantially higher contribution to the overall strength in comparison with carbide precipitation in the carbon-doped alloys. The ductility of the alloys decreased slightly with increasing carbon content. Finally, a decrease in the testing temperature to 77 K strongly improved both the strength and ductility of the program alloys.

CRediT authorship contribution statement

M. Klimova: Investigation, Writing - review & editing, Visualization, Supervision. **D. Shaysultanov:** Investigation. **A. Semenyuk:** Investigation. **S. Zherebtsov:** Methodology, Writing - review & editing. **N. Stepanov:** Writing - original draft, Visualization, Supervision, Funding acquisition.

Declaration of competing interest

The authors declare that they have no known competing financial interests or personal relationships that could have appeared to influence the work reported in this paper.

Acknowledgements

References

[1] J.W. Yeh, S.K. Chen, S.J. Lin, J.Y. Gan, T.S. Chin, T.T. Shun, C.H. Tsau, S.Y. Chang, Nanostructured high-entropy alloys with multiple principal elements: novel alloy design concepts and outcomes, Adv. Eng. Mater. 6 (2004) 299−303, https://doi.org/10.1002/adem.200300567.

[2] D.B. Miracle, O.N. Senkov, A critical review of high entropy alloys and related concepts, Acta Mater. 122 (2017) 448−511, https://doi.org/10.1016/j.actamat.2016.08.081.

[3] O.N. Senkov, D.B. Miracle, K.J. Chaput, Development and exploration of refractory high entropy alloys — a review, J. Mater. Res. (2018), https://doi.org/10.1557/jmr.2018.153.

[4] Y. Zhang, T. Ting, Z. Tang, M.C. Gao, K.A. Dahmen, P.K. Liaw, Z. Ping, Progress in materials science microstructures and properties of high-entropy alloys, J. Prog. Mater. Sci. 61 (2014) 1−93, https://doi.org/10.1016/j.pmatsci.2013.10.001.

[5] S. Gorsse, D.B. Miracle, O.N. Senkov, Mapping the world of complex concentrated alloys, Acta Mater. 135 (2017) 177−187, https://doi.org/10.1016/j.actamat.2017.06.027.

[6] Y. Lu, Y. Dong, S. Guo, L. Jiang, H. Kang, T. Wang, B. Wen, Z. Wang, J. Jie, Z. Cao, H. Ruan, T. Li, A promising new class of high-temperature alloys: eutectic high-entropy alloys, Sci. Rep. 4 (2014) 1−5, https://doi.org/10.1038/srep06200.

[7] O.N. Senkov, G.B. Wilks, D.B. Miracle, C.P. Chuang, P.K. Liaw, Refractory high-entropy alloys, Intermetallics 18 (2010) 1758−1765, https://doi.org/10.1016/j.intermet.2010.05.014.

[8] O.N. Senkov, G.B. Wilks, J.M. Scott, D.B. Miracle, Mechanical properties of Nb 25Mo 25Ta 25W 25 and V 20Nb 20Mo 20Ta 20W 20 refractory high entropy

alloys, Intermetallics 19 (2011) 698–706, https://doi.org/10.1016/j.intermet.2011.01.004.

[9] O.N. Senkov, S. Gorsse, D.B. Miracle, High temperature strength of refractory complex concentrated alloys, Acta Mater. 175 (2019) 394–405, https://doi.org/10.1016/J.ACTAMAT.2019.06.032.

[10] Z. Wu, H. Bei, G.M. Pharr, E.P. George, Temperature dependence of the mechanical properties of equiatomic solid solution alloys with face-centered cubic crystal structures, Acta Mater. 81 (2014), https://doi.org/10.1016/j.actamat.2014.08.026.

[11] B. Cantor, I.T.H. Chang, P. Knight, A.J.B. Vincent, Microstructural development in equiatomic multicomponent alloys, Mater. Sci. Eng. A. 375–377 (2004) 213–218, https://doi.org/10.1016/j.msea.2003.10.257.

[12] F. Otto, A. Dlouhý, C. Somsen, H. Bei, G. Eggeler, E.P. George, The influences of temperature and microstructure on the tensile properties of a CoCrFeMnNi high-entropy alloy, Acta Mater. 61 (2013) 5743–5755, https://doi.org/10.1016/j.actamat.2013.06.018.

[13] A. Gali, E.P. George, Tensile properties of high- and medium-entropy alloys, Intermetallics 39 (2013) 74–78, https://doi.org/10.1016/j.intermet.2013.03.018.

[14] B. Gludovatz, A. Hohenwarter, D. Catoor, E.H. Chang, E.P. George, R.O. Ritchie, A fracture-resistant high-entropy alloy for cryogenic applications, Science (80-.) 345 (2014) 1153–1158, https://doi.org/10.1126/science.1254581.

[15] Z. Zhang, M.M. Mao, J. Wang, B. Gludovatz, Z. Zhang, S.X. Mao, E.P. George, Q. Yu, R.O. Ritchie, Nanoscale origins of the damage tolerance of the high-entropy alloy CrMnFeCoNi, Nat. Commun. 6 (2015) 10143, https://doi.org/10.1038/ncomms10143.

[16] B. Gludovatz, A. Hohenwarter, K.V.S. Thurston, H. Bei, Z. Wu, E.P. George, R.O. Ritchie, Exceptional damage-tolerance of a medium-entropy alloy CrCoNi at cryogenic temperatures, Nat. Commun. 7 (2016) 1–8, https://doi.org/10.1038/ncomms10602.

[17] Z. Zhang, H. Sheng, Z. Wang, B. Gludovatz, Z. Zhang, E.P. George, Q. Yu, S.X. Mao, R.O. Ritchie, Dislocation mechanisms and 3D twin architectures generate exceptional strength-ductility-toughness combination in CrCoNi medium-entropy alloy, Nat. Commun. 8 (2017), https://doi.org/10.1038/ncomms14390.

[18] G. Laplanche, A. Kostka, C. Reinhart, J. Hunfeld, G. Eggeler, E.P. George, Reasons for the superior mechanical properties of medium-entropy CrCoNi compared to high-entropy CrMnFeCoNi, Acta Mater. 128 (2017) 292–303, https://doi.org/10.1016/j.actamat.2017.02.036.

[19] N. Stepanov, M. Tikhonovsky, N. Yurchenko, D. Zyabkin, M. Klimova, S. Zherebtsov, A. Efimov, G. Salishchev, Effect of cryo-deformation on structure and properties of CoCrFeNiMn high-entropy alloy, Intermetallics 59 (2015) 8–17, https://doi.org/10.1016/j.intermet.2014.12.004.

[20] Z. Wang, I. Baker, Interstitial strengthening of a f.c.c. FeNiMnAlCr high entropy alloy, Mater. Lett. 180 (2016), https://doi.org/10.1016/j.matlet.2016.05.122.

[21] Z. Wang, I. Baker, W. Guo, J.D. Poplawsky, The effect of carbon on the microstructures, mechanical properties, and deformation mechanisms of thermo-mechanically treated Fe40.4Ni11.3Mn34.8Al7.5Cr6 high entropy alloys, Acta Mater. 126 (2017) 346–360, https://doi.org/10.1016/j.actamat.2016.12.074.

[22] Z. Li, C.C. Tasan, H. Springer, B. Gault, D. Raabe, Interstitial atoms enable joint twinning and transformation induced plasticity in strong and ductile high-entropy alloys, Sci. Rep. 7 (2017) 1–7, https://doi.org/10.1038/srep40704.

[23] M. Wang, Z. Li, D. Raabe, In-situ SEM observation of phase transformation and twinning mechanisms in an interstitial high-entropy alloy, Acta Mater. 147 (2018) 236–246, https://doi.org/10.1016/j.actamat.2018.01.036.

[24] I. Baker, Interstitials in f.c.c. high entropy alloys, Metals 10 (2020) 1–20, https://doi.org/10.3390/met10050695.

[25] Z. Li, Interstitial equiatomic CoCrFeMnNi high-entropy alloys: carbon content, microstructure, and compositional homogeneity effects on deformation behavior, Acta Mater. 164 (2019) 400–412, https://doi.org/10.1016/j.actamat.2018.10.050.

[26] J. Chen, Z. Yao, X. Wang, Y. Lu, X. Wang, Y. Liu, X. Fan, Effect of C content on microstructure and tensile properties of as-cast CoCrFeMnNi high entropy alloy, Mater. Chem. Phys. 210 (2018) 136–145, https://doi.org/10.1016/j.matchemphys.2017.08.011.

[27] L.B. Chen, R. Wei, K. Tang, J. Zhang, F. Jiang, L. He, J. Sun, Heavy carbon alloyed FCC-structured high entropy alloy with excellent combination of strength and ductility, Mater. Sci. Eng. A. (2018), https://doi.org/10.1016/j.msea.2018.01.045.

[28] J.Y. Ko, S.I. Hong, Microstructural evolution and mechanical performance of carbon-containing CoCrFeMnNi-C high entropy alloys, J. Alloys Compd. 743 (2018) 115–125, https://doi.org/10.1016/j.jallcom.2018.01.348.

[29] Z. Wang, I. Baker, Z. Cai, S. Chen, J.D. Poplawsky, W. Guo, The effect of interstitial carbon on the mechanical properties and dislocation substructure evolution in Fe40.4Ni11.3Mn34.8Al7.5Cr6 high entropy alloys, Acta Mater. (2016), https://doi.org/10.1016/j.actamat.2016.08.072.

[30] N.D. Stepanov, N.Y. Yurchenko, M.A. Tikhonovsky, G.A. Salishchev, Effect of carbon content and annealing on structure and hardness of the CoCrFeNiMn-based high entropy alloys, J. Alloys Compd. 687 (2016) 59–71, https://doi.org/10.1016/j.jallcom.2016.06.103.

[31] N.D. Stepanov, D.G. Shaysultanov, R.S. Chernichenko, N.Y. Yurchenko, S.V. Zherebtsov, M.A. Tikhonovsky, G.A. Salishchev, Effect of thermomechanical processing on microstructure and mechanical properties of the carbon-containing CoCrFeNiMn high entropy alloy, J. Alloys Compd. 693 (2017)

[32] Z. Wu, C.M. Parish, H. Bei, Nano-twin mediated plasticity in carbon-containing FeNiCoCrMn high entropy alloys, J. Alloys Compd. 647 (2015) 815–822, https://doi.org/10.1016/j.jallcom.2015.05.224.

[33] I. Moravcik, J. Cizek, L. Gouvea, J. Cupera, I. Guban, I. Dlouhy, Nitrogen interstitial alloying of CoCrFeMnNi high entropy alloy through reactive powder milling, Entropy 21 (2019) 363, https://doi.org/10.3390/e21040363.

[34] D. Edgard Jodi, J. Park, N. Park, Strengthening of ultrafine-grained equiatomic CoCrFeMnNi high-entropy alloy by nitrogen addition, Mater. Lett. (2019) 126772, https://doi.org/10.1016/j.matlet.2019.126772.

[35] D. Edgard, J. Park, B. Straumal, N. Park, Investigation on the precipitate formation and behavior in nitrogen-containing equiatomic CoCrFeMnNi high-entropy alloy, Mater. Lett. 258 (2020) 126806, https://doi.org/10.1016/j.matlet.2019.126806.

[36] F. Xiong, R. Fu, Y. Li, D. Sang, Effects of nitrogen alloying and friction stir processing on the microstructures and mechanical properties of CoCrFeMnNi high- entropy alloys, J. Alloys Compd. 822 (2020) 153512, https://doi.org/10.1016/j.jallcom.2019.153512.

[37] Z. Li, H.H. Lee, S.H. Shim, J.H. Jang, Short-range order strengthening in boron-doped high-entropy alloys for cryogenic applications, Acta Mater. (2020), https://doi.org/10.1016/j.actamat.2020.04.052.

[38] M.V. Klimova, D.G. Shaysultanov, R.S. Chernichenko, V.N. Sanin, N.D. Stepanov, S.V. Zherebtsov, A.N. Belyakov, Recrystallized microstructures and mechanical properties of a C-containing CoCrFeNiMn-type high-entropy alloy, Mater. Sci. Eng. A. (2019) 740–741, https://doi.org/10.1016/j.msea.2018.09.113, 201–210.

[39] D. Shaysultanov, N. Stepanov, S. Malopheyev, I. Vysotskiy, V. Sanin, S. Mironov, R. Kaibyshev, G. Salishchev, S. Zherebtsov, Friction stir welding of a carbon-doped CoCrFeNiMn high-entropy alloy, Mater. Charact. 145 (2018) 353–361, https://doi.org/10.1016/J.MATCHAR.2018.08.063.

[40] H. Cheng, H.Y. Wang, Y.C. Xie, Q.H. Tang, P.Q. Dai, Controllable fabrication of a carbide-containing FeCoCrNiMn high-entropy alloy: microstructure and mechanical properties, Mater. Sci. Technol. 33 (2017) 2032–2039, https://doi.org/10.1080/02670836.2017.1342367.

[41] M.V. Klimova, A.O. Semenyuk, D.G. Shaysultanov, G.A. Salishchev, S.V. Zherebtsov, N.D. Stepanov, Effect of carbon on cryogenic tensile behavior of CoCrFeMnNi-type high entropy alloys, J. Alloys Compd. 811 (2019) 152000, https://doi.org/10.1016/j.jallcom.2019.152000.

[42] M. S, L. Guo, X. Ou, S. Ni, Y. Liu, Effects of carbon on the microstructures and mechanical properties of FeCoCrNiMn high entropy alloys, Mater. Sci. Eng. A. 746 (2019) 356–362, https://doi.org/10.1080/14786435.2017.1369191.

[43] L. Guo, J. Gu, X. Gong, K. Li, S. Ni, Y. Liu, M. Song, Short-range ordering induced serrated flow in a carbon contained FeCoCrNiMn high entropy alloy, Micron 126 (2019), https://doi.org/10.1016/j.micron.2019.102739.

[44] J. Peng, Z. Li, L. Fu, X. Ji, Z. Pang, A. Shan, Carbide precipitation strengthening in fine-grained carbon-doped FeCoCrNiMn high entropy alloy, J. Alloys Compd. (2019), https://doi.org/10.1016/J.JALLCOM.2019.06.204.

[45] M.V. Klimova, D.G. Shaysultanov, S.V. Zherebtsov, N.D. Stepanov, Effect of second phase particles on mechanical properties and grain growth in a CoCrFeMnNi high entropy alloy, Mater. Sci. Eng. A. (2019), https://doi.org/10.1016/j.msea.2019.01.112.

[46] Z. Wang, W. Lu, D. Raabe, Z. Li, On the mechanism of extraordinary strain hardening in an interstitial high-entropy alloy under cryogenic conditions, J. Alloys Compd. 781 (2019) 734–743, https://doi.org/10.1016/J.JALLCOM.2018.12.061.

[47] Z. Wang, H. Bei, I. Baker, Microband induced plasticity and the temperature dependence of the mechanical properties of a carbon-doped FeNiMnAlCr high entropy alloy, Mater. Charact. 139 (2018) 373–381, https://doi.org/10.1016/j.matchar.2018.03.017.

[48] N.D. Stepanov, D.G. Shaysultanov, M.S. Ozerov, S.V. Zherebtsov, G.A. Salishchev, Second phase formation in the CoCrFeNiMn high entropy alloy after recrystallization annealing, Mater. Lett. 185 (2016) 1–4, https://doi.org/10.1016/j.matlet.2016.08.088.

[49] F. Otto, A. Dlouhý, K.G. Pradeep, M. Kuběnová, D. Raabe, G. Eggeler, E.P. George, Decomposition of the single-phase high-entropy alloy CrMnFeCoNi after prolonged anneals at intermediate temperatures, Acta Mater. 112 (2016) 40–52, https://doi.org/10.1016/j.actamat.2016.04.005.

[50] F.J. Humphreys, M. Hatherly, Recrystallization and Related Annealing Phenomena, Elsevier, 2004.

[51] N. Louat, The resistance to normal grain growth from a dispersion of spherical particles, Acta Metall. 30 (1982) 1291–1294, https://doi.org/10.1016/0001-6160(82)90147-X.

[52] M. Hillert, Inhibition of grain growth by second-phase particles, Acta Metall. 36 (1988) 3177–3181, https://doi.org/10.1016/0001-6160(88)90053-3.

[53] T. Gladman, Precipitation hardening in metals, Mater. Sci. Technol. 15 (1999) 30–36, https://doi.org/10.1179/026708399773002782.

[54] Z. Wang, A. Genc, I. Baker, Direct versus indirect particle strengthening in a strong, ductile FeNiMnAlTi high entropy alloy, Mater. Charact. 132 (2017) 156–161, https://doi.org/10.1016/j.matchar.2017.08.019.

[55] P.M. Hazzledine, Direct versus indirect dispersion hardening, Scr. Metall. Mater. 26 (1992) 57–58.

[56] A. Saeed-Akbari, J. Imlau, U. Prahl, W. Bleck, Derivation and variation in composition-dependent stacking fault energy maps based on subregular solution model in high-manganese steels, Metall. Mater. Trans. A Phys. Metall. Mater. Sci. 40 (2009) 3076–3090, https://doi.org/10.1007/s11661-009-0050-8.

[57] M. Klimova, N. Stepanov, D. Shaysultanov, R. Chernichenko, N. Yurchenko, V. Sanin, S. Zherebtsov, Microstructure and mechanical properties evolution of the Al, C-containing CoCrFeNiMn-type high-entropy alloy during cold rolling, Materials 11 (2017) 1−14, https://doi.org/10.3390/ma11010053.

[58] W. Guo, J. Su, W. Lu, C.H. Liebscher, C. Kirchlechner, Y. Ikeda, F. Körmann, X. Liu, Y. Xue, G. Dehm, Dislocation-induced breakthrough of strength and ductility trade-off in a non-equiatomic high-entropy alloy, Acta Mater. 185 (2020) 45−54, https://doi.org/10.1016/j.actamat.2019.11.055.

[59] O. Bouaziz, S. Allain, C.P. Scott, P. Cugy, D. Barbier, High manganese austenitic twinning induced plasticity steels : a review of the microstructure properties relationships, Curr. Opin. Solid State Mater. Sci. 15 (2011) 141−168, https://doi.org/10.1016/j.cossms.2011.04.002.

[60] G. Laplanche, A. Kostka, O.M. Horst, G. Eggeler, E.P. George, Microstructure evolution and critical stress for twinning in the CrMnFeCoNi high-entropy alloy, Acta Mater. 118 (2016) 152−163, https://doi.org/10.1016/j.actamat.2016.07.038.

[61] V. Gerold, H.P. Karnthaler, On the origin of planar slip in f.c.c. alloys, Acta Metall. 37 (1989) 2177−2183, https://doi.org/10.1016/0001-6160(89)90143-0.